CIRP Journal of Manufacturing Science and Technology 62 (2025) 24–37

Contents lists available at ScienceDirect

CIRP Journal of Manufacturing Science and Technology

journal homepage: www.elsevier.com/locate/cirpj

The role of material properties in modeling maximal surface temperatures and heat distribution in milling of UD CFRP

Wolfgang Hintze, Ganna Shchegel, Jan Mehnen, Carsten Möller *, Jan Dege

Institute of Production Management and Technology, Hamburg University of Technology, Denickestraße 17, Hamburg 21073, Germany

ARTICLE INFO

Keywords:
CFRP
Milling
Moving heat source
Surface damage
Temperature
Heat flow
Fibre orientation angle

ABSTRACT

In order to meet the precision requirements for components made of carbon fibre reinforced plastics (CFRP), the edges are often trimmed by milling. However, this can lead to detrimental thermal damage to the machined surface. The aim of the study was to investigate in detail the maximum temperatures and characteristic thermal parameters for various unidirectional CFRP materials under different cutting conditions. During upcut milling using a PCD cutter an infrared camera, thermocouples and a dynamometer were employed to monitor temperatures and the cutting power. An analytical heat flow model suitable for arbitrary fibre orientation angles was used to determine, based on thermal material properties, the temperature change at the machined surface and the heat flow parameters from experiments. Material influence on the cutting power was considered by its specific elastic energy at fracture depending on the volume content and mechanical properties of the fibres. At the machined surface, the resin glass transition temperatures were frequently exceeded, and the highest temperature changes were observed at a fibre orientation angle of $\Phi = 135°$. In most cases, higher cutting speeds were accompanied by greater temperature changes. Phenomenological models of the thermal parameters of the machining process were developed, which take into account both the thermal and mechanical CFRP properties and show a good correlation with the experimental results. They provide benefits in order to predict the temperature fields for materials with differing properties and under varying cutting conditions.

1. Introduction and state of the art

Carbon fibre-reinforced plastics (CFRP) have become indispensable as the foundation of technological solutions for reducing structural weight and increasing strength in aerospace, ground and marine vehicles, medicine, and sports. Their high mechanical strength, which depends on the orientation of the fibre reinforcement relative to the applied load, makes them highly beneficial for use in finished structures. However, it also imposes significant demands on equipment and technological processes during production [1,2].

Mechanical chip-removal machining is typically applied at the final stage of the component production chain, when near-net-shape workpieces still require contouring or, less frequently, surface machining to achieve the necessary dimensional accuracy and surface quality for subsequent assembly operations [2]. Insufficient processing quality necessitates costly sorting and rejection of defective or substandard materials and workpieces. The machining process characteristics vary significantly depending on the selected machining parameters [3]. This is primarily due to the highly heterogeneous and anisotropic properties of CFRP components, which consist of mechanically distinct phases of fibres and matrix [4].

An important challenge in machining CFRP lies in selecting optimal parameters, ensuring that the applied forces effectively cut the fibres while preserving the undegraded matrix's ability to provide structural support under conditions of machining-induced heat exposure [5]. The importance of selecting appropriate cutting conditions to avoid thermal damage in CFRP is emphasized in [6,7]. In [8], the influence of selected cutting parameters on cutting forces and the quality of the machined surface is studied in the context of drilling metal-GFRP stacks. Material removal mechanisms of unidirectional CFRP at different fibre cutting angles are considered in [9–12] and their relation to temperature distribution in [13,14]. Reference [7] classifies approaches to studying temperature changes into two main categories: those based on force measurements and those that measure temperature directly. Temperature measurements are usually carried out using thermocouples positioned at a certain distance from the machined edge or by means of infrared thermography [15–19]. Optimization algorithms and inverse problem-solving approaches for estimating the intensity of moving heat sources in transient heat conduction problems were considered in [16,

* Corresponding author.
E-mail address: c.moeller@tuhh.de (C. Möller).

https://doi.org/10.1016/j.cirpj.2025.08.002
Received 16 April 2025; Received in revised form 17 July 2025; Accepted 1 August 2025
Available online 27 August 2025

Nomenclature

$a_{e,eff}$	effective width of cut.
$a_{e,nom}$	nominal width of cut.
a_p	depth of cut.
C_p	specific heat capacity.
d_t	tool diameter.
f	feed.
h	chip thickness.
K_0	modified Bessel function of the second kind of order zero.
k_{11}	thermal conductivity in 1st orthotropic direction parallel to fibres.
k_{33}	thermal conductivity in 2nd orthotropic direction perpendicular to fibres.
n	number of spindle revolutions pro unit time.
l_m	length of machined path.
P_c	cutting power.
P_{HS}	heat flow into the workpiece.
q_{HS}	heat flux of the heat source.
r_β	radius of the tool cutting-edge.
R_W	ratio of the heat flow from the heat source into the workpiece to the cutting power.
S	integration variable.
s_{HS}	thermal contact length of the heat source.
T_g	glass transition temperature.
v_c	cutting speed.
v_f	feed rate and heat source velocity.
x_{HS}	horizontal position of the centre of the heat source.
x_n	horizontal coordinate of the point of interest for which the temperature is modelled.
z	distance from the machined surface to the infrared camera measurement line.
z_n	vertical coordinate of the point of interest for which the temperature is modelled.
ΔT_{max}	maximum temperature change.
ζ_Φ	fibre orientation symmetry angle.
θ	fibre cutting angle.
ρ_w	density.
Φ	fibre orientation angle.
φ	engagement angle.

20,21].

Numerous strategies to counteract temperature increase have been proposed and investigated, including specialized tool coatings, the use of coolants and cryogenic approaches, and alternative cutting methods [22–24]. Nevertheless, there are many applications where trimming part contours by dry milling remains advantageous due to its technological efficiency, the absence of coolant residues on finished parts, and the overall high processing performance of the method [1,25,26].

Detailed approaches to modeling the machined surface temperature increase are provided in [13,21,27–29], whereas the advantage of the approach developed in [21] is that the direction of tool motion along the machined surface can be set at an arbitrary angle to the material's orthotropic directions. A considerable amount of elastic energy released upon fibre breakage as well as energy dissipation due to friction lead to significant heating of both the tool and the workpiece, often exceeding the matrix's glass transition temperature even under moderate machining conditions [30,31]. Several studies have shown that this deterioration in the matrix's mechanical properties and its ability to support the fibres directly correlates with the extent of machined surface damage [15,32,33].

In [34], the influence of thermoplastic vs. thermoset matrix of carbon fibre reinforced composites on temperatures in drilling was studied. It was found, that thermoplastic matrix results in higher hole wall and chip temperatures presumably due to continuous non-brittle chips morphology and consequently longer tool-chip contact length and thrust force. At the same time, the higher delamination damage of CFRP with thermoset matrix was presumably due to lower interlaminar toughness.

In [26], an analytical model incorporating fibre orientation-dominated thermal anisotropy was developed to investigate the thermal field in the machined surface layer during dry milling of unidirectional CF/PEEK. A moving arc surface heat source was considered; however, the model was established only for fibre orientations of 0°, 45°, 90°, and 135°.

It should be noted that different definitions of the fibre orientation angle are found in the literature. While the 0° and 90° directions coincide across definitions, the 45° and 135° directions represent opposite situations depending on the chosen convention. One approach defines the fibre orientation angle as the angle between the feed rate vector v_f and the fibre direction on the cut-off side of the unidirectionally reinforced panel relative to the machined surface, as seen in [26,35,36] etc. Alternatively, it can be defined relative to the fibre direction on the bulk side of the panel [1,13,21,37–39], which is the convention followed in the present work.

In [40], the influence of cutting on the mechanical and thermal material properties was studied, for which a model based on the finite element modeling (FEM) considering both heat flux and modulus degradation in cutting was developed. In [41] a FEM model for milling of GFRP was developed and the influence of cutting parameters was investigated. In [42], the heat flux of different materials like metal, concrete, and ceramic composites were estimated using combined FEM and Carslaw and Jaeger approach. In [43], the influence of the width of cut as well as the fibre orientation angle was investigated using a FEM-based approach. The study examined the effects of machining parameters on temperature, but only for a specific unidirectional CFRP material tested. In [37], the influence of various fibre orientation angles, including 22.5°, 67.5°, 112.5°, and 157.5°, was analyzed using a combined analytical and experimental approach. In [38], the same methodology was applied to investigate the influence of tool type on temperature rise during dry CFRP trimming.

Thus, while other aspects of CFRP machining have been extensively researched, the influence of CFRP material properties on surface heating during machining remains an area requiring further investigation [25].

The aim of this study was therefore to investigate in detail the maximum temperatures and characteristic thermal parameters for various unidirectional (UD-) CFRP materials under different cutting conditions. Factors such as fibre volume content, which defines the ratio of highly abrasive, high-strength fibres to the thermally sensitive matrix, and corresponding material density may significantly affect heating. Additionally, thermal material properties, including specific heat capacity and highly direction-dependent thermal conductivity, play a crucial role in regulating heat accumulation and distribution within the workpiece. The present study focuses on investigating the form, characteristics and extent of these effects taking into account both thermal and mechanical constituent influences and their interconnection.

To achieve this aim, a combined experimental and analytical approach was employed. Sections 2.1–2.4 describe the materials and machining setup under consideration, as well as the experimental methods used. Section 2.5 is dedicated to the analytical model used to calculate the maximum temperature increase at the machined surface. Section 3 presents the analysis of both experimental and modeling results. It begins with a detailed explanation of the analysis steps performed and then discusses the influence of material properties on the mechanical aspects of the machining process. Specifically, it concerns the cutting power, as it is the key physical quantity introduced into the

system during machining and is partially converted into heat.

Subsequent subsections of Section 3 examine the influence of material properties on the modeled maximum temperature increase at the machined surface, the thermal parameters determined via the combined experimental and analytical approach, and the portion of cutting power that contributes to heating the material. The results are then generalized in the form of phenomenological dependencies of the thermal parameters on material properties. By knowing the thermal parameters, which are derived from material and machining properties, it becomes possible to calculate the temperature fields and maximum temperature increases for given processing conditions.

Finally, the modeled temperature fields are graphically visualized, and the results are compared with relevant findings from the literature.

2. Materials and methods

Four different UD-CFRP materials were tested in dry upcut milling at varying fibre orientations in three test series each characterized with one of two levels of cutting speed, feed and width of cut. Subsequent simulations of the temperature fields were conducted based on the temperatures measured at several distances from the cutting surface using thermocouples and an infrared camera.

2.1. Materials

The material specification includes autoclave curing of prepregs that combine epoxy matrix and carbon fibres. The material's thermal conductivity and glass transition temperature were experimentally determined and are provided in Table 1. Other properties are given according to [37] and manufacturer data [44].

CFRP 3 and 4 have higher fibre volume content ϑ_{FVC} as well as higher density ρ_w and thermal conductivity k_{11} and k_{33} in both directions of orthotropy compared to CFRP 1 and 2. Higher pressure applied during autoclave curing of CFRP 1 compared to 2 resulted in a slightly higher fibre volume content ϑ_{FVC}. CFRP 2 is also characterized with a higher specific heat capacity C_p than CFRP 1. Among the materials of higher ϑ_{FVC}, CFRP 3 has a lower specific heat capacity C_p than CFRP 4. CFRP 3 differs from CFRP 1 and 2 with the matrix used. CFRP 4 has different fibres and matrix compared to other materials. Matrixes of both CFRP 3 and 4 are characterized by the manufacturer as exhibiting high damage tolerance and impact resistance. Materials CFRP 1 to 3 are characterized with the same Young modulus E and strength R_m of fibres, which are lower than E and R_m of CFRP 4. Specific elastic energy at fracture W_{el} is calculated as described in Section 3 and is related to E, R_m and ϑ_{FVC}.

2.2. Tools

In accordance with industrial practice experiments were conducted using upcut milling with work-sharp double-edged polycrystalline diamond (PCD) cutters. Such cutters provide comparatively longer service life compared to uncoated tools and do not suffer from coating chipping. Moreover, they can be sharpened up to several times. The parameters of the tools are listed in Table 2. The tool of bigger diameter was used only for the material of the type 4 for comparison. Tools of smaller diameters were not tested as their shafts are severely prone to brittle mechanical failure in bending even under moderate feed speeds making it hardly possible to reach the industrially demanded high material processing rates. Even tools of the selected diameters are highly influenced by heating especially during longer processing times [1,40], but it was not investigated in this study.

The provided low number of cutting edges for the selected tools as well as sufficient clearance angle provide better heat evacuation in contact with the surrounding and lower friction, thus reducing the thermal loading of the material investigated. Low rake and helix angles indirectly provide higher wedge angle of the tools and therefore higher strength of the tool teeth making them less prone to breaking under high mechanical and thermal loadings.

The radius of the tool cutting edge was measured after carrying out series of tests. For an initially new tool, the radius was typically close to $r_\beta = 20$ µm after the first machined path of $l_m = 300$ mm and remained less than $r_\beta = 30$ µm before the used maximum machined path of $l_m = 1.5$ m. The tool geometry therefore was assumed to be constant in this range.

As the length of the tool cutting edge along the tool axis was 22 mm, it allowed repeated use of the cutting edge for processing of machined path of higher total length due to choosing several separate regions along the tool cutting edge. The thickness of the tested CFRP-panels was equal to the depth of cut $a_p < 5$ mm. This allowed for the use of three separate regions of the cutting edge, each approximately 7 mm in width. Each of them was used for the cutting length of maximally 1.5 m.

Table 2
Geometry of the double-edged polycrystalline diamond peripheral milling tool.

Parameter	Symbol	Value	Unit
Tool diameter	d_t	12 – CFRP 1, 2, 3 (14 – CFRP 4)	mm
Number of cutting edges	z_t	2	-
Clearance angle	α_f	12	°
Rake angle	γ_f	0	°
Helix angle	δ	0	°

Table 1
Material properties of the CFRP panels.

Parameter	Symbol	Values for each type of material				Unit
No. of material CFRP		1	2	3	4	
Fibres		HTS	HTS	HTS	T800	
Matrix		HexPly 913	HexPly 913	HexPly 6376	HexPly M21	
Density	ρ_w	1517	1514	1584	1594	kg/m^3
Fibre volume content	ϑ_{FVC}	52	50	58	60	%
Specific heat capacity	C_p	892.4	994.9	867.8	922.3	J/(kg • K)
Thermal conductivity in 1st directions of orthotropy (parallel to fibres)	k_{11}	7.695	7.472	8.569	8.483	$\frac{W}{m \bullet K}$
Thermal conductivity in 2nd directions of orthotropy (perpendicular to fibres)	k_{33}	0.630	0.612	0.702	0.725	$\frac{W}{m \bullet K}$
Glass transition temperature	T_g	150.1	150.1	162.1	161.8	°C
Number of UD-layers	n_l	16	16	16	22	-
Panel thickness (equal to depth of cut)	a_p	4.716	4.772	4.159	4.019	mm
E-module of fibres	E	238	238	238	294	GPa
Strength of fibres	R_m	4.3	4.3	4.3	5.49	GPa
Specific elastic energy at fracture	W_{el}	20.2	19.4	22.5	30.6	$\frac{mJ}{mm^3}$

2.3. Process parameters

Processing parameters were chosen to be possibly close to the values usually chosen in industrial practice in order to provide maximal possible processing rates under reliable mechanical and thermal performance of the tool and the processed material [9,23], though the exact relationships between the latter factors are the subject of the present investigation. On the other side, the values chosen were restricted with the parameters of the machining center used for the experiments. Table 3 gives the used process parameters. To provide a reliable comparison between materials of varying properties, the same test series were carried out for each of the tested materials. To still investigate the influence of the tool diameter, a tool of the same type but of bigger diameter d_t was used for CFRP 4. Test series TS-I and TS-II differed in the cutting speed v_c and therefore in the feed rate v_f but were characterized with the same other parameters, in particular the same feed f. TS-III was realized with the same cutting speed v_c as the TS-II but in partial cut, i.e. with a lower nominal width of cut $a_{e,nom}$. The relations between the cutting speed v_c and the feed f were chosen in such a way that two levels of each parameter were tested and the same material removal rate Q_W was provided in the TS-I and TS-III.

Each test series included investigation of the influence of the fibre orientation angle Φ between the feed rate vector v_f and the fibre direction of the UD-reinforced panels on the bulk side of the panel relative to the provided machined surface, i.e. not on the panel's cut-off side (as shown in Fig. 1). A similar definition is also applied to the fibre cutting angle θ defined between the directions of fibres and cutting speed v_c as shown in Fig. 1, b. To realize it, the CFRP rectangular specimens were prepared with fibres readily placed at corresponding angles to the side. Therefore, a straight cut of the length equal to the panel side dimension parallel to it was provided in each experiment. Tested values of Φ are given in Table 3 and include the case of fibres perpendicular to the machined surface with $\Phi = 90°$ and two cases of symmetrical orientation to the perpendicular direction, i.e. $\Phi = 45°$ and $\Phi = 135°$ with corresponding fibre orientation symmetry angle ζ_Φ [37]:

$$\zeta_\Phi = |\Phi - 90°| = 45° \quad (1)$$

In a number of preliminary tests, as well as in previous studies [37,38], it was shown that cutting at a fibre orientation of $\Phi = 0°$ leads to immediate fracture of the unidirectionally reinforced panel when using the test setup. This is due to the low inter-fibre fracture strength of the UD material. Adding additional strengthening layers was not possible, as it was necessary to maintain free access to both sides of the panel for temperature measurement using an infrared camera and for installing thermocouples, as described in the following section. Moreover, additional layers would have interfered with the cutting power measurements and compromised the comparability of the results. Therefore, the fibre orientation $\Phi = 0°$ was excluded from this study.

Table 3
Investigated range of machining parameters(*).

Parameter	Symbol	Values in test series (TS)			Unit
Test series number		TS-I	TS-II	TS-III	
Cutting speed	v_c	100	450	450	$\frac{m}{min}$
Feed	f	0.06	0.06	0.107	mm
Feed rate	v_f	0.159 (0.136)	0.716 (0.614)	1.273 (1.091)	$\frac{m}{min}$
Nominal width of cut	$a_{e,nom}$	12 (14)	12 (14)	1.5 (1.75)	mm
Material removal rate	Q_W	9.55	42.97	9.55	$\frac{cm^3}{min}$
Fibre orientation angle	Φ	45 / 90 / 135	45 / 90 / 135	45 / 90 / 135	°

(*) data is given for CFRP 1, 2, 3; data for CFRP 4 is given in parentheses

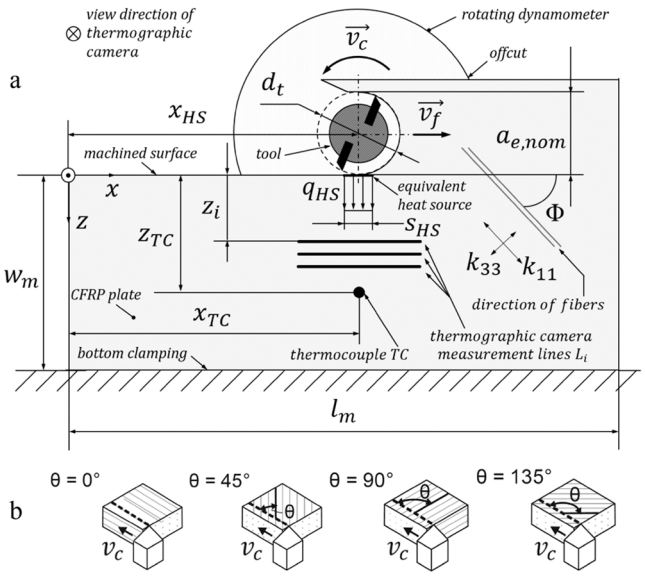

Fig. 1. Schematic representation of the machining situation of the CFRP-panels (a) and definition of the fibre cutting angle (b).

2.4. Test scheme and measurement equipment

To realize the test series described above, the test scheme as in Fig. 1 was used. Panels of the tested materials were installed vertically to provide the necessary fibre orientation angle Φ to the feed rate direction of the horizontally moving spindle with rotating dynamometer and tool. This allowed frontal access for the infrared camera with no obstacles such as the spindle itself, tool or chips, which could prevent monitoring of temperatures normally to the panel surface. The infrared camera moved together with the spindle so that it was always centered relative to the tool. This allowed continuous measuring of temperatures along imaginary horizontal lines with the infrared camera as depicted in Fig. 1. Three such lines were chosen at distances z_i from the machined surface to provide redundancy of experimental data and therefore compensating possible random errors. A thermocouple was additionally installed at the distance z_{TC} from the machined surface, which was chosen to be small enough to measure higher temperature increases but safe to avoid damages by the tool.

The measured temperatures were followingly used for modelling the tool interacting with the material as a heat source of width s_{HS} and heat flux q_{HS}, as depicted in Fig. 1. The initial temperature of the composite panels prior to machining, that is, the ambient temperature, was also measured in advance and subtracted from the recorded data. The following analysis was based on assumption of a uniform surrounding temperature. The ambient temperature ranged from 18 °C to 32 °C on different testing days. The influence of the initial temperature on the development of temperature increases during machining could not be accounted for, nor could the effects of humidity or other environmental factors. This is due to the machining center being equipped with an open processing chamber, which would require significant design modifications to maintain constant initial temperature and/or humidity conditions.

The length of cut l_m was from 21 to 25 times the diameter of the cutting tool d_t. Table 4 provides selected values for the setup arrangement. The panels were clamped from the bottom side. To ensure a uniform clamping force distribution over the clamped area of 0.015 m², a robust metallic traverse with a thin plastic coating on the contact surface was used. This setup provided both rigid contact and vibration damping, while also thermally isolating the panels from the metal holders, which have higher thermal conductivity.

Table 4
Setup parameters for modeling and experiments.

Parameter	Symbol	Value	Unit
Length of machined path	l_m	300	mm
Distance in transversal direction from cutting surface to workpiece clamp	w_m	50	mm
Horizontal distance to TC	x_{TC}	177.8	mm
Vertical distance from machined surface to TC	z_{TC}	1.5	mm
Distances to the lines of measurement with the infrared camera	z_i	0.7 / 0.92 / 1.38	mm
Nominal width of cut:			
- for CFRP 1, 2, 3	$a_{e.nom}$	1.5 / 12	mm
- for CFRP 4	$a_{e.nom}$	1.75 / 14	mm

The processing module of the 5-axis machining center Reichenbacher VISION II-Sprint with the installed setup corresponding to the machining situation is shown in Fig. 2, which also shows side and front views of the tool used. Although a straight cutting path was used in this study, the flexibility in selecting the motion direction provided by the 5-axis machining center enabled optimal access for temperature measurement systems on both sides of the panels. The spindle was equipped with a 4-component rotating dynamometer Kistler Typ 9170A with a signal conditioner Kistler Typ 5238B for measuring torque M_z and calculating corresponding mechanical processing power P_c. The torque measurement accuracy was 0.1 Nm. The influence of hot chips on the workpiece temperature was minimized with the chips vacuuming system Schuko, which provided suction capacity of 13600 m^3 /h.

The temperature of the CFRP-panel in the vicinity of the tool was measured with a frontally positioned infrared camera Micro-Epsilon ThermoIMAGER TIM VGA 640 × 480 px, 32 Hz, noise equivalent temperature difference NETD 40 mK, as well as a shielded thermocouple of type J (Fe/CuNi) by TC Direct with the hot junction of the thermocouple placed in a specially drilled hole in the CFRP-panel on the side opposite to the side monitored with the infrared camera. The hole was of 0.6 mm diameter and 2 mm depth filled with a thermal conducting paste. The thermocouple diameter d_{tc}= 0.5 mm defines the maximum achievable spatial resolution of the temperature measurement, as it defines the minimum physical area over which temperature can be accurately recorded. The thermocouples operated at a sampling rate of f_s= 100 Hz,

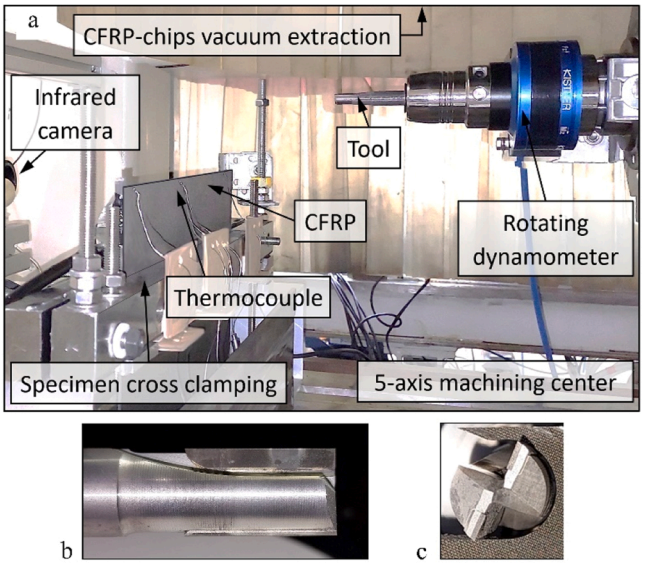

Fig. 2. Experimental setup (a), including infrared camera, thermocouple, and rotating dynamometer, as well as the tool used (b, c – side and front views).

resulting in a time interval between successive measurements of $\Delta t_{tc} = 1/f_s$. The sampling time interval Δt_{tc} also limits the maximum achievable spatial resolution of the temperature measurement, as it determines the distance $l_{tc} = v_f \bullet \Delta t_{tc}$ the heat source and the corresponding temperature field moves between successive readings. According to the minimal and maximal feed rate v_f, the distance l_{tc} is between 0.02 and 0.2 mm and thus the resolution is limited by the thermocouple diameter d_{tc}.

To determine the infrared emissivity of the CFRP material, separate tests were performed, whereas an external heating source was used to heat the specimens. The values measured with thermocouples were compared to the data obtained with the infrared camera. An emissivity value of $\xi_m = 0.95$ was selected for the temperature range of 30 °C to 140 °C, keeping the average temperature error below 3 °C. Similar CFRP materials are characterized with the range of emissivity values, which aligns with the selected one [45,46]. Higher temperatures were intentionally avoided to prevent exceeding the glass transition temperature and corresponding thermal degradation of the panel.

Additional check of the thermometric camera measurements by comparing them with the temperatures measured with the thermocouple showed that deviation between the temperature values measured with both methods did not exceed 4 °C, that complies with the accuracy of the used devices.

2.5. Analytical modeling

The region of the tool and material interaction was modelled as a moving strip heat source of heat flux q_{HS}, length s_{HS}, width a_p and zero depth in a plane of the machined surface (Fig. 1). Temperature fields due to moving heat sources were investigated in [13,21,26,27,37,38]. The heat liberation is modelled to take place across the heat source area and represents the combined result of occurring heat producing processes such as material cutting, different damage modes, cracks opening, friction etc. In this study, the strip-shaped heat source of constant heat flux is considered substituting the actual periodic heat flux provided in the case of discontinuous cutting edge engagement. This approximation is possible due to the high speed of revolutions corresponding to the selected cutting speed v_c.

The followingly cut-off regions of material panels are neglected as well as heat exchange with the surrounding, convection and radiation. The real processed panel with tool, chips and cut-off is substituted with the semi-infinite solid with adiabatic surface except of the region where the heat source is acting. In this case, the two-dimensional model for an infinite width of the heat source and corresponding thickness of the tested material panel can be utilized with no heat conduction in the direction normal to the processed panel, i.e. to the coodinate plane (x, z) (see Fig. 1). The influence of these simpifying assumptions is taken into account by the resulting value of the heat source parameters, i.e. heat flux q_{HS} and length s_{HS} of the introduced moving heat source.

This approach makes it possible to compare similar machining scenarios for different materials within the framework of the same modeling methodology, even in practical machining scenarios characterized with heat dissipation and finite workpiece dimensions. It should be noted that accounting for subsequent cut-off regions of the material panels, as well as heat losses to the surroundings, could lead to even higher values of the thermal contact parameters. This is because such adjustments would compensate for the fact that, despite additional heat losses, the experimentally measured temperatures in the vicinity of the cutting surface still reach the values observed in the tests.

The benefit of the previously developed analytical model [21,37,38] is an explicit consideration of the effects of fibre orientation, as they play a core role in determining the thermal behaviour of CFRP. The model gives the following temperature distribution in the plane (x_n, z_n) of the CFRP panel resulting from the action of the moving strip source in a steady state due to machining the panel along its edge at arbitrary fibre

orientation angle Φ:

$$\Delta T(x_n,\quad z_n) = K_q \int_{x_n - s_{HS}/2}^{x_n + s_{HS}/2} \exp\Big(K_s\big[(k_{11}-k_{33})\big(S \quad \bullet \cos^2\Phi + z_n \bullet \sin\Phi \bullet \cos\Phi\big) - k_{11} \bullet S\big]\Big) \bullet K_0\Big\{K_s \bullet \big(k_{11} - (k_{11}-k_{33}) \quad \bullet \cos^2\Phi\big)^{1/2}\big[(k_{11}-k_{33}) \bullet \big((z_n^2 - S^2) \bullet \cos 2\Phi - 2z_n \bullet S \bullet \sin\Phi \bullet \cos\Phi\big) + k_{11} \bullet S^2 + k_{33} \bullet z_n^2\big]^{1/2}\Big\} dS \tag{2}$$

where

$$K_q = \frac{q_{HS}}{\pi\sqrt{k_{11}k_{33}}} \tag{3}$$

$$K_s = \frac{\rho_w C_p v_f}{2k_{11}k_{33}} = \frac{\rho_w C_p}{2\pi k_{11}k_{33}} \bullet \frac{v_c \bullet f}{d_t} \tag{4}$$

K_0 is the modified Bessel function of the second kind of order zero, S is the integration variable $S = x_n - x_{HS}$, and the main direction of orthotropy coincides with the fibre reinforcement direction and is defined with the fibre orientation angle Φ. Other symbols are given in nomenclature above.

Knowing experimentally measured maximum temperature changes and according distances to the machined surface, relevant for the material and the tested machining situation, q_{HS} and s_{HS} were identified by solving the nonlinear least-squares problem to fit the model in Eq. (2), see in Section 3. Their product gives the value of the heat flow P_{HS} as follows:

$$P_{HS} = s_{HS} \bullet q_{HS} \bullet a_p. \tag{5}$$

The measured value of the torque M_z was used to calculate the mechanical power of material processing:

$$P_c = 2 \bullet M_z \bullet \frac{v_c}{d_t}. \tag{6}$$

The portion of the mechanical processing power P_c that is converted into heating of the machined panel is given by the ratio of heat flow to cutting power:

$$R_W = P_{HS}/P_c. \tag{7}$$

To be able to predict the temperature change ΔT at the machined surface, additional phenomenological dependencies of q_{HS} and s_{HS} from the thermal and mechanical material parameters and cutting conditions were identified and empirically modelled based on the obtained experimental and calculated data. The corresponding phenomenological dependencies are described below in Section 3.5.

The initial model formulation in [27] considers heat distribution into a semi-infinite half-space from a moving heat source of an infinite width. As a result, the temperature is assumed to be exactly twice as high as in the case of a fully infinite space, since the same heat flux q_{HS} is distributed into a geometrically two times smaller domain. In the model described by Eqs. (2–4), the heat generated by the unit-width heat source is likewise distributed over a unit-width slice of the half-space. Under the conditions considered in this article, this assumption holds, as the heat source width is equal to the panel width. Heat exchange with the surroundings is neglected, i.e., the panel sides are treated as adiabatic surfaces.

It is important to note, however, that for future considerations involving three-dimensional heat distribution under oblique cutting conditions, where the “heat distribution slice” is bounded by the actual structure’s geometry, greater heat accumulation should be expected, since heat cannot dissipate beyond the structural boundaries. This would require an appropriate correction of the K_q coefficient. Due to the limited size of the domain available for heat distribution, as opposed to the infinite domain assumed in the original model in [27], experimentally observed temperatures are likely to be higher than in the idealized case. This may result in an overestimation of the q_{HS} or s_{HS} parameters if the same estimation procedure is applied. Nonetheless, this problem can be addressed experimentally by significantly increasing heat exchange with the surroundings, for example, through liquid cooling. In that case, implementing of a suitable heat exchange model would be necessary.

3. Results and discussion

The tests carried out provided the data concerning the temperatures and torques during milling of four types of UD-CFRP materials, which differ in the fibres/matrices used or in their physical properties as listed above in Table 1.

The thermal parameters of the cutting process result from the conversion of the cutting power introduced during the process into heat. As the cutting performance is directly dependent on the mechanical material properties, these also have an influence on the thermal parameters. Therefore, in the first step, the dependence of the cutting power on the mechanical material properties is investigated.

Secondly, temperature data and thermal material properties were used to calculate the equivalent heat flux q_{HS} and the thermal contact length s_{HS} corresponding to the tested machining process using the measured temperatures within Eq. (2) according to the physically based model of the moving heat source.

Considering the temperatures measured at different testing conditions and for varying materials, it should be noted, that the Bayesian posterior mean of the standard deviation σ did not exceed 9 K for all the tests. This corresponds to a maximum Bayesian posterior standard error of the mean equal to not more than 5 K, computed as $t \bullet \sigma/\sqrt{n}$, where n is the number of measurements per test condition, and t is the appropriate quantile from the Student’s t-distribution. The prior distributions for the mean and variance (i.e., prior variance of the mean, and prior shape and scale parameters for the variance) were assumed to be the same for all test conditions.

The values of q_{HS} and s_{HS} were then used for simulation of full temperature fields in the vicinity of the machined surface according to Eq. (2), also in points where the temperature could not be measured experimentally due to proximity to the processing milling tool. As a first step, the simulated maximum temperature increases ΔT_{max} at the distances z_i and z_{TC} (see Table 4) from the machined surface were compared to the values measured using the infrared camera and thermocouples, respectively. The calculated root mean square error was RMSE = 6.7 °C, which can be attributed to uncertainties in thermocouple positioning, estimation of the infrared camera’s observation point, the influence of surrounding areas on infrared measurements, particularly under strong temperature gradients, as well as the spatial resolution limitations of both measurement methods. Then, the simulated maximum temperature changes ΔT_{max} at the machined surface were calculated and the influence of material properties or parameters as listed in Table 1 as well as process parameters as included in Eqs. (2–4) analyzed.

As a result, empirical models for the q_{HS} and s_{HS} are developed on the basis of the phenomenological relationships found between the mechanical and thermal material properties on the one hand and the cutting power and the thermal parameters q_{HS} and s_{HS} on the other.

Finally, the heat flow ratio R_W was calculated according to Eq. (7) together with Eqs. (5) and (6).

3.1. Influence of the material on the cutting power

The cutting behavior of CFRP with thermoset matrix can be characterized as brittle because of the negligible plastic strains of both fibres and matrix. Accordingly, the ultimate strength approximately coincides with the yield strength. Chip formation occurs as soon as the yield strength is reached. It can therefore be assumed that the energy required to produce chips depends on the elastic properties of the respective materials.

The volume-related elastic energy W_{el} at fracture of a brittle material is determined from the ultimate strength R_m and modulus of elasticity E as follows [47]:

$$W_{el} = (R_m)^2/(2E) \tag{8}$$

Regarding the CFRP materials with thermoset matrix the different properties as well as the fibre content must be taken into account. Since the volume-related elastic energy of the matrix according to calculations is less than 1 % of the volume-related elastic energy of the fibres, it can be neglected. However, the volume-related elastic energy of the composite is affected by the fibre volume content ϑ_{FVC} and can thus be expressed by

$$W_{el} = \vartheta_{FVC} \bullet (R_m)^2/(2E) \tag{9}$$

where R_m and E are the fibre properties. The volume-related elastic energies of the CFRP material are given in Table 1.

The theoretical power for complete separation of a brittle material can be calculated by multiplying the volume-related elastic energy W_{el} with the material removal rate Q_W:

$$P_{th} = W_{el} \bullet Q_W \tag{10}$$

The material removal rate Q_W should take into account the real tool engagement. As it will be described below, large-scale material breakouts were observed under certain conditions in all the tested materials leading to a reduced effective width of cut $a_{e,eff}$ compared to the nominal one $a_{e,nom}$. Appropriate material removal rate is

$$Q_{W,eff} = f \bullet v_c \bullet a_{e,eff} \bullet a_p/(\pi \bullet d_t) \tag{11}$$

where the variables correspond to the ones given in the nomenclature. Therefore, the theoretical power of brittle fracture

$$P_{th,eff} = W_{el} \bullet Q_{W,eff} \tag{12}$$

can be used as a characteristic parameter to differentiate the brittle fracture behavior of individual materials during a specific cutting process.

As Fig. 3 shows, the theoretical power of brittle fracture $P_{th,eff}$ correlates with the measured cutting power P_c for the investigated CFRP materials. The coefficients of determination are $R^2 = 0.97$ for a common dependency for materials CFRP 1, 2 and 3, $R^2 = 0.95$ for CFRP 4. Thus, the specific elastic energy at fracture W_{el} can be taken as an indicator for the material influence on the cutting power. A different slope of the regression line is observed for CFRP 4 compared to the other CFRP materials possibly due to the different tool diameters used in cutting (see Table 2) and therefore due to slightly differing engagement conditions.

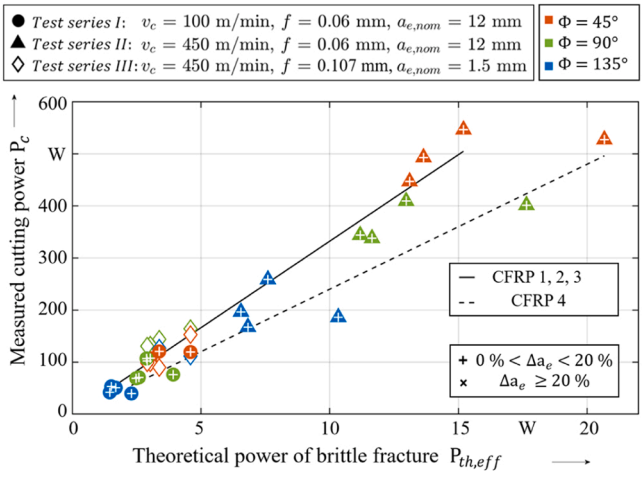

Fig. 3. Measured cutting power P_c vs. theoretical power of brittle fracture $P_{th,eff}$ based on fibre mechanical and material composition properties of the investigated CFRP.

3.2. Temperature changes ΔT_{max} for all materials and test series

Simulated values of the maximum temperature changes ΔT_{max} at the machined surface for the four tested materials are shown in Fig. 4. According marks indicate the maximum temperature changes, which correspond to reaching the glass transition temperature of the matrix T_g. It can be seen that T_g was exceeded for all materials in all test series at the fibre orientation angle $\Phi = 135°$. For each separately considered test series, the maximum temperature changes ΔT_{max} are highest at $\Phi = 135°$ for all materials. For all CFRPs, material break-outs have been observed in full cut, i.e. in TS-I and TS-II, irrespective of the cutting speed v_c leading to reduced effective width of cut $a_{e,eff}$. The classification of resulting relative changes in the width of cut Δa_e is given in Fig. 4 as well as specified in Section 3.3. It has to be pointed out, that although $a_{e,eff}$ is lowest at $\Phi = 135°$ due to the largest material breakouts, the highest temperature changes occur here.

This observation aligns with previous research findings, which report that the highest cutting forces occur at approximately $\theta = 135°$ [1,2]. This can be attributed to the approximate alignment between the direction of the active cutting forces and the material's fibre orientation. Such alignment results in greater elastic energy accumulation prior to fracture, due to the high tensile strength of fibres along their longitudinal axis. Additionally, frictional forces in this configuration act nearly parallel to the fibre direction, contributing to increased local stresses and greater energy dissipation.

Considering CFRP 1 and CFRP 2, these materials mainly differ in the specific heat capacity due to different consolidation routes. For CFRP 1 and CFRP 2, higher ΔT_{max} for $\Phi = 135°$ are reached at the higher cutting speed $v_c = 450$ m/min in TS-II and TS-III. For other fibre orientation angles Φ, T_g was also exceeded in most cases for CFRP 1 and some of them for CFRP 2, with higher temperatures observed at the higher cutting speed v_c, particularly in full cut (TS-II). Among the mentioned tests, higher temperature changes were predominantly observed at $\Phi = 45°$ than at $\Phi = 90°$. This might be to one hand due to increased heating during each tool rotation, which is mainly influenced by the force acting at the engagement angle range corresponding to the maximum chip thickness. Accordingly in case of $\Phi = 45°$ the corresponding active force at $\theta = 135°$ is much higher than the active force in case of $\Phi = 90°$ at $\theta = 0°$. On the other hand, the high thermal conductivity k_{11} along fibres promotes heat distribution in the more distant areas of material in case of fibres directed normally to the machined surface at $\Phi = 90°$ in contrast to a higher heat accumulation close to the machined surface at $\Phi = 45°$.

A comparison of CFRP 1 with CFRP 2, where the latter has the same type of matrix and fibres but mainly a higher C_p, shows correspondingly lower ΔT_{max} for CFRP 2 in almost all cases.

Another pattern of ΔT_{max} dependency on processing conditions is observed for CFRP 3. Compared to CFRP 1, CFRP 3 has another type of matrix, considerably higher fibre volume content and accordingly higher density, thermal conductivity and glass transition temperature.

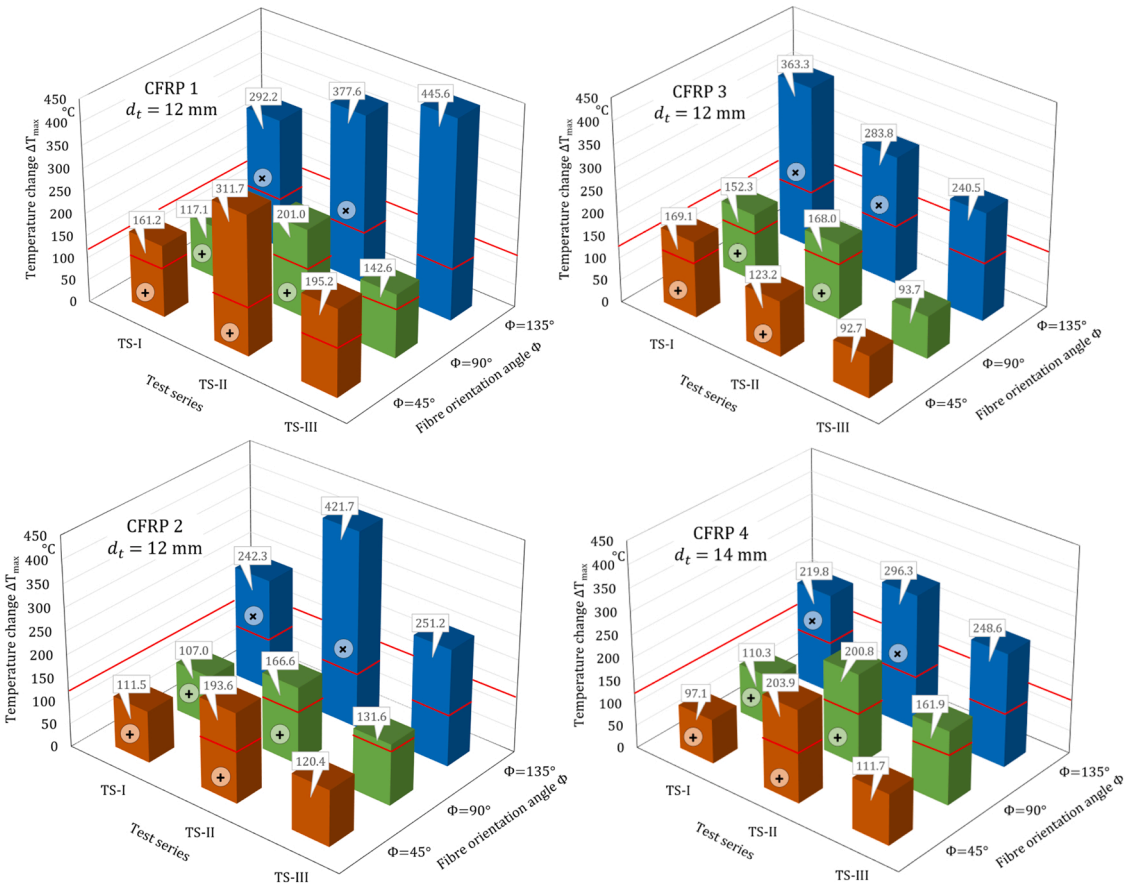

Fig. 4. Simulated maximum temperature changes at machined surface ΔT_{max} depending on material, machining parameters according to the test series TS-I, II, III as indicated in Table 3, and fibre orientation angles Φ, whereas relative reduction in the width of cut 0 % $< \Delta a_e <$ 20 % is marked with a "+ " sign, and $\Delta a_e \geq$ 20 % with a "× " sign as described in Section 3.3.

In case of CFRP 3, higher ΔT_{max} are observed in full cut, i.e. in TS-I and TS-II, compared to partial cut in TS-III. The highest ΔT_{max} for CFRP 3 at $\Phi = 45°$ and $\Phi = 135°$ occurs at the lower v_c (TS-I). For CFRP 3, the partial cut at the higher cutting speed v_c (TS-III) is characterized with lower temperatures at the machined surface, compared to other test series at the same Φ. Across test series, tests at $\Phi = 45°$ and $\Phi = 90°$ for CFRP 3 do not indicate a clear dependency on the fibre orientation angle and are characterized with similar ΔT_{max}.

CFRP 4 is characterized with a less pronounced increase of the maximum temperature changes ΔT_{max} at $\Phi = 135°$, compared to the other materials. Nevertheless, it demonstrates comparatively higher ΔT_{max} often exceeding the glass transition temperature of the matrix T_g at the higher cutting speed v_c similarly to the materials CFRP 1 and 2. Similarly to how it predominantly occurs in the mentioned materials, the highest ΔT_{max} is observed in TS-II in full cut.

Compared to test series TS-I, test series TS-III is characterized by a significantly higher cutting speed v_c with the same material removal rateQ_W but correspondingly reduced engagement values $a_{e,nom}$ and f, which is generally characterized as high-speed machining. Contrary to the advantage of lower cutting surface temperatures known from

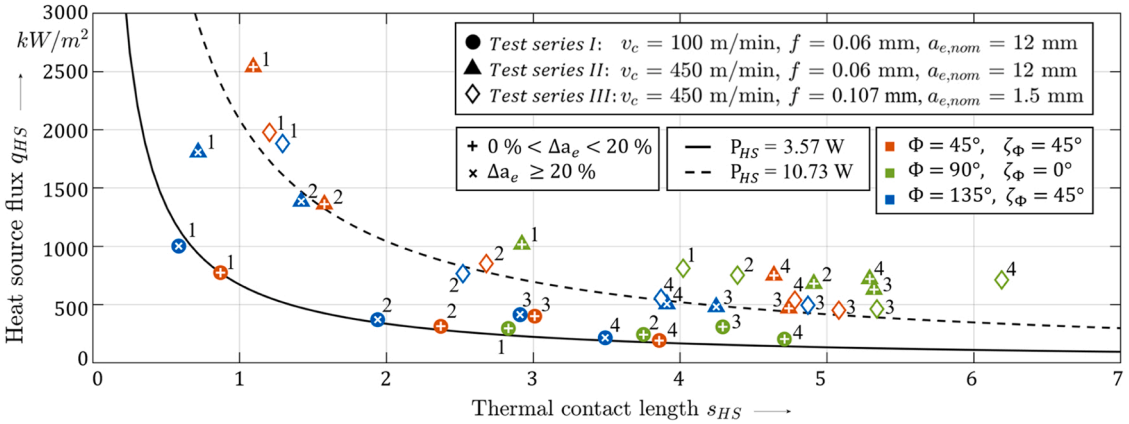

Fig. 5. Equivalent heat flux q_{HS} vs. thermal contact length s_{HS} at varying cutting speeds v_c, feeds f, nominal widths of cut $a_{e,nom}$ and fibre orientation angles Φ. 1, 2, 3, 4 – No. of material CFRP (see Table 1).

metallic materials, this is not the case with the CFRP materials analyzed in the tested cutting speed range. It can be seen that the temperature changes ΔT_{max} are rather high in the case of TS-III for all CFRPs except for the CFRP 3, for which ΔT_{max} are always higher in the TS-I.

In some cases, the matrix decomposition temperature T_d was reached, which for the CFRP 1 and CFRP 2 is equal to approximately 410 °C [38]. The influence of the matrix decomposition is not covered by the model, but the affected zone is considerably smaller than the one, where T_g is reached.

The differences in thermal as well as mechanical properties of investigated CFRP materials as they are seen from Table 1 seem to provide complicated mutual effects leading to non-uniform dependencies of temperature changes on the test series and fibre orientation angles.

3.3. Thermal parameters s_{HS} and q_{HS} for all materials and test series

Fig. 5 depicts the relationship between the heat flow P_{HS}, the equivalent heat source flux q_{HS} and the thermal contact length s_{HS} according to the Eg. (5). Thermal contact lengths s_{HS} of the tested materials ranges from ca. 0.5 mm to 6.5 mm and equivalent heat source flux q_{HS} from ca. 100 kW/m² to some more than 2500 kW/m². For all tested materials, the tests at the lower cutting speed v_c = 100 m/s (TS-I) are characterized with generally lower values of q_{HS} than at the higher cutting speed v_c = 450 m/s (TS-II and TS-III). In contrast, s_{HS} is less effected by the cutting conditions of the test series.

This applies even taking into account the difference in the nominal $a_{e,nom}$ and actually observed effective width of cut $a_{e,eff}$. The relative changes in the width of cut $\Delta a_e = (a_{e,nom} - a_{e,eff})/a_{e,nom}$ were classified and indicated in Figs. 3 – 7. The reason for the changes Δa_e in width of cut during machining is a break-out of large-scale material particles of UD-CFRP panels on the cut-off side [37]. It occurs along the direction of reinforcing fibres due to tensile stresses perpendicular to the fibre reinforcement created by the cutting force. Break-outs occurring at corresponding cutting-edge engagement angles φ result in accordingly observed changes in the width of cut Δa_e, which are therefore higher for the fibre orientation angle $\Phi = 135°$. For all the tested materials, higher Δa_e relate to minimal values of s_{HS} according to simulations. Due to the small nominal width of cut $a_{e,nom}$, in partial cut the possible break-outs were not observed.

As already described in [37], the pairs of values (s_{HS}, q_{HS}) for both $\Phi = 45°$ and $\Phi = 135°$ are observed at higher q_{HS} and lower s_{HS} and closer to each other compared to the corresponding pairs of values for $\Phi = 90°$. This observation can be expressed with the fibre orientation symmetry angle ζ_Φ according to the Eq. (1). For the case of $\zeta_\Phi = 0°$ (i.e. for $\Phi = 90°$), generally higher s_{HS} are observed than for $\zeta_\Phi = 45°$ (i.e. for

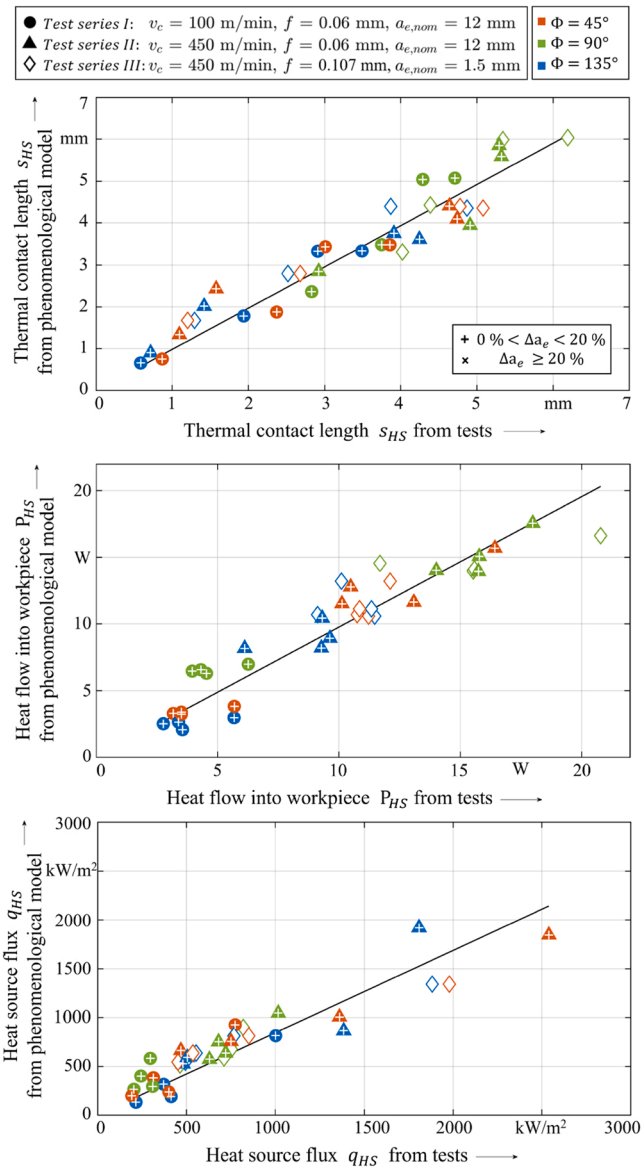

Fig. 7. Thermal contact length s_{HS}, heat flow P_{HS}, equivalent heat flux q_{HS} determined using phenomenological dependencies in Eqs. (13, 14) and Eq. (5) vs. determined in tests using the analytical model in Eqs. (2–4).

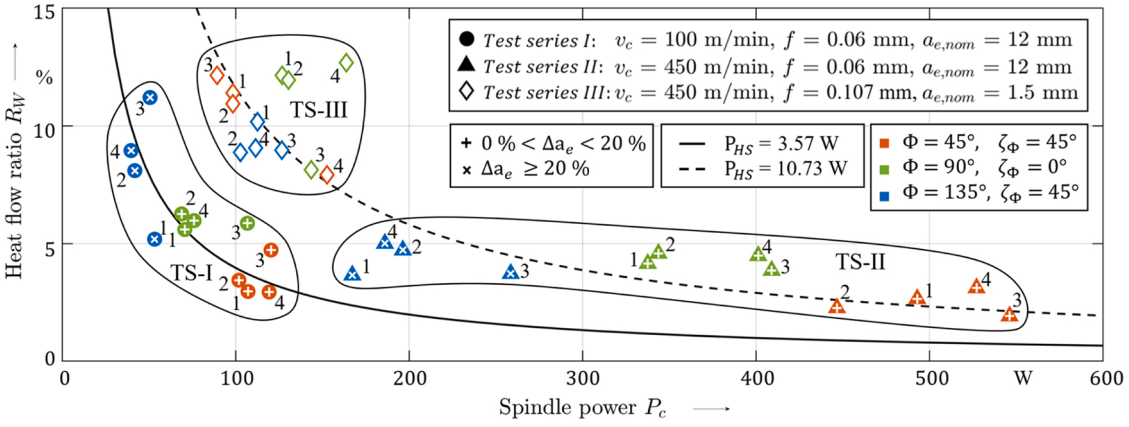

Fig. 6. Heat flow ratio R_W vs. spindle power P_c at varying cutting speeds v_c, feeds f, nominal widths of cut $a_{e,nom}$ and fibre orientation angles Φ for the tested materials. 1, 2, 3, 4 – No. of material CFRP (see Table 1).

$\Phi = 45°$ and $\Phi = 135°$) for each separately considered material and test series.

It should be noted that the experimentally determined parameters s_{HS} and q_{HS} show no clear dependence on the feed rate v_f, although v_f appears in Eqs. (2) and (4). But as it will be shown later in Section 3.6, the heat flow P_{HS}, which is proportional to the product of s_{HS} and q_{HS} (see Eq. 5), shows phenomenological proportionality to v_f.

3.3.1. Compare CFRP 1 to CFRP 2 – s_{HS}, q_{HS} and P_{HS}

The thermal contact length of the heat source s_{HS} of CFRP 2 is higher than that of CFRP 1 in all test series, but q_{HS} of CFRP 2 is mostly lower than q_{HS} of CFRP 1. Corresponding pairs of points (s_{HS}, q_{HS}) of CFRP 1 and CFRP 2 at the same cutting speed are arranged on hyperbolas, i.e. curves of the same heat flow P_{HS}. Thus, the higher specific heat capacity C_p of CFRP 2 not only leads to lower temperature changes ΔT_{max} (Fig. 4), but also to lower q_{HS} and higher s_{HS} (Fig. 5). These observations are not immediately apparent from Eq. (2) due to the interrelationship between the parameters. As expected, due to mechanical properties, the cutting power P_c is similar for the both materials (Table 1 in Section 2.1 and Fig. 6 in Section 3.4).

3.3.2. Compare CFRP 3 to CFRP 1 and 2 – s_{HS}, q_{HS} and P_{HS}

CFRP 3 differs from CFRP 1 and 2 in its matrix composition and a higher fibre volume content resulting in higher ρ_w, k_{11}, k_{33} and lower C_p as well as slightly higher W_{el}. Again, as in the case of materials CFRP 1 and 2, the values of P_{HS} are predominantly dependent on the cutting speed v_c, i.e. are similar for the TS-II and TS-III.

CFRP 3 compared to CFRP 1 and 2 leads to a slightly higher heat flow P_{HS} in TS-I. In TS-II and TS-III, the pairs of points (s_{HS}, q_{HS}) are shifted towards higher s_{HS} and lower q_{HS} compared to CFRP 1 and CFRP 2. This may indicate that interaction of thermal and mechanical material properties considerably influences s_{HS}, q_{HS} and P_{HS}.

3.3.3. Compare CFRP 4 to CFRP 1, 2 and 3 – s_{HS}, q_{HS} and P_{HS}

CFRP 4 differs from other tested CFRPs in its type of fibres and matrix composition and has a fibre volume content similar to CFRP 3. For CFRP 4, ρ_w, k_{11}, k_{33} are similar to those of CFRP 3 and higher than those of CFRP 1 and 2. For CFRP 4, C_p is higher than for CFRP 1 and 3, but lower than for CFRP 2, that can be explained with the differing fibres and matrix composition. The tests for CFRP 4 were conducted with a tool of the same type but a higher diameter d_t with corresponding feed rate v_f according to the constant v_c and f, width of cut $a_{e,nom}$ was equal to d_t in full cut and $a_{e,nom} = 0.125 \bullet d_t$ in partial cut (see Tables 2 and 3). Like for all other tested materials, the values of P_{HS} for CFRP 4 are predominantly dependent on the cutting speed v_c and are similar for the TS-II and TS-III, whereas the influence of v_f is superimposed with the influence of other parameters.

CFRP 4 at v_c= 100 m/min leads to a similar heat flow P_{HS} compared to CFRP 1 and 2 but lower than for CFRP 3. At $v_c = 450$ m/min P_{HS} is on average slightly higher than for other CFRPs. The corresponding pairs of points (s_{HS}, q_{HS}) at the same cutting speed are often arranged closer to the corresponding points for CFRP 3 and shifted to higher values of s_{HS} and lower q_{HS} compared to CFRP 1 and 2.

These observations cannot be easily explained with thermal or mechanical properties considered separately, but indicate tight interactions between their influences.

In addition, in Fig. 5, hyperbolas of constant heat flow according to Eq. (5) are depicted. Apparently, the heat flow predominantly corresponds to the value of the cutting speed v_c. Thus, in TS-I at the lower cutting speed v_c, the value of P_{HS} determined with least-squares fitting across all the tested materials is 3.57 W. In TS-II and TS-III at the higher cutting speed v_c, the appropriate P_{HS} is about 10.73 W.

3.4. Cutting power P_c and heat flow ratio R_w

For the material-specific choice of thermally favorable cutting conditions, the extent to which the applied cutting power is converted into heat is of interest.

With regard to the measured cutting power P_c, it was found that the material type is of secondary importance compared to the other factors analyzed. P_c is dominated by the cutting conditions differing between TS-I, II and III. Moreover, in full cut, i.e. in TS-I and TS-II, for all materials, the lowest P_c is at the fibre orientation angle $\Phi = 135°$, intermediate at $\Phi = 90°$, and the highest at $\Phi = 45°$. This can be explained with the highest uncut chip thickness occurring at the fibre cutting angle $\theta = 45°$ in the case of $\Phi = 135°$ and the highest uncut chip thickness occurring at the fibre cutting angle $\theta = 135°$ in the case of $\Phi = 45°$, whereas the highest cutting forces occur at approximately $\theta = 135°$ [1, 2]. Concerning dependency on the machining parameters, as expected, the cutting power P_c increases in the full cut under otherwise constant conditions, when the cutting speed v_c is increased from TS-I to TS-II.

Irrespective of the material, comparing test series TS-I and TS-III under identical material removal rate Q_W, P_c in full cut in TS-I is mostly slightly lower than in partial cut in TS-III. The differences in the measured spindle power can partly be addressed to the reduced effective width of cut $a_{e,eff}$ due to fibre break outs, already reported in [37], see marked symbols in Fig. 6.

The heat flow ratio R_W is described by Eq. (7). Corresponding dependencies of R_W on measured cutting power P_c are shown in Fig. 6. Delimited value ranges of (P_c, R_W) are shown for the three test series in Fig. 6, but no obvious difference between the CFRP materials is apparent. In particular, it is clear that higher heat flows P_{HS} are observed in the partial cut at the higher cutting speed v_c and feed rate v_f, i.e. in TS-III, compared to the full cut at the lower cutting speed v_c and feed rate v_f, i.e. in TS-I, at the same material removal rate. This again indicates that in the investigated speed range, high speed cutting is thermally unfavorable.

3.5. Phenomenological dependencies of q_{HS} and s_{HS}

Concluding the experimentally obtained observations, it is reasonable to assume, that the characteristic thermal parameters equivalent heat flux q_{HS} and thermal contact length s_{HS} mainly depend on material thermal and mechanical parameters as well as on the cutting conditions. They are density ρ, thermal conductivities k_1 and k_3, thermal capacity C_p, fibre volume content ϑ_{FVC} and specific elastic energy at fracture W_{el}, fibre orientation angle Φ, fibre orientation symmetry angle ζ_Φ, cutting speed v_c and feed f, theoretical power of brittle fracture $P_{th,eff}$.

Thus, the equivalent heat flux q_{HS} and the thermal contact length s_{HS}, which were determined with the analytical model in Eqs. (2–4) based on experimental data in different test series as listed in Table 3, were used to establish a phenomenological model to describe the dependency of q_{HS} and s_{HS} on the material properties of the workpiece and the machining parameters.

The Levenberg-Marquardt nonlinear least squares algorithm [48] was utilized to obtain the corresponding nonlinear regression coefficients of the thermal parameters on the parameters mentioned as predictors. The empirically determined dependency of s_{HS} is as follows:

Table 5
Coefficients of the thermal contact length s_{HS} nonlinear regression model.

Predictor	Estimate	95 % CI (Lower, Upper)
β_0	$0.11 \bullet 10^2$	[11.111, 11.176]
β_1 (v_c)	0.32	[0.267, 0.374]
β_2 ($v_c^{\sqrt{2}/2}$)	– 2.28	[–2.657, –1.902]
β_3 (f)	21.73	[21.726, 21.728]
β_4 (ζ_Φ)	– 0.04	[–0.045, –0.028]
β_5 (d_t)	– 0.69	[–1.030, –0.348]
β_6 ($C_p \bullet \rho$)	$0.11 \bullet 10^{-4}$	$[0.075, 0.148] \bullet 10^{-4}$
β_7 ($k_1 \bullet k_{33}$)	$0.21 \bullet 10^{-1}$	[1.687, 2.469]
β_8 ($P_{th,eff}$)	0.06	[0.021, 0.106]

$$\begin{aligned} s_{HS} \;=\; & 0.11 \bullet 10^2 \mathrm{mm} + \; 0.32 \; \frac{\mathrm{mm} \bullet \mathrm{min}}{\mathrm{m}} \\ & \bullet v_c - 2.28 \; \frac{\mathrm{mm} \bullet \mathrm{min}^{\sqrt{2}/2}}{\mathrm{m}^{\sqrt{2}/2}} \bullet v_c^{\sqrt{2}/2} \; + \; 21.73 \; \frac{\mathrm{mm}}{\mathrm{mm}} \\ & \bullet f - 0.04 \; \frac{\mathrm{mm}}{^\circ\mathrm{deg}} \bullet \zeta_\Phi - 0.69 \; \frac{\mathrm{mm}}{\mathrm{mm}} \\ & \bullet d_t \; + \; 0.11 \bullet 10^{-4} \; \frac{\mathrm{mm} \bullet \mathrm{kg} \bullet \mathrm{K} \bullet \mathrm{m}^3}{\mathrm{J} \bullet \mathrm{kg}} \bullet C_p \bullet \rho + \; 0.21 \\ & \bullet 10^{-1} \frac{\mathrm{mm} \bullet \mathrm{m}^2 \bullet \mathrm{K}^2}{\mathrm{W}^2} \bullet k_1 \bullet k_{33} \; + \; 0.06 \; \frac{\mathrm{mm} \bullet \mathrm{m} \bullet \mathrm{K}}{\mathrm{W}} \bullet P_{th,eff} \end{aligned} \tag{13}$$

Here the components ($C_p \bullet \rho$) and ($k_1 \bullet k_{33}$) are chosen following the analytical model in Eq. (2). For the phenomenological dependency in Eq. (13), the coefficient of determination is $R^2 = 0.91$. The confidence intervals at the 95 % confidence level of the appropriate coefficients are given in Table 5.

It turned out that the dependency of q_{HS} from the parameters is sufficiently expressed by means of preliminary empirical modelling of P_{HS} and s_{HS}, where P_{HS} can be expressed as follows:

$$\begin{aligned} P_{HS} \;=\; & 0.18 \bullet 10^4 \mathrm{W} + \; 0.29 \bullet 10^3 \; \frac{\mathrm{W}}{\mathrm{mm}} \\ & \bullet f \; + \; 0.249 \; \frac{\mathrm{W} \bullet \mathrm{min}^{\sqrt{2}/2}}{\mathrm{m}^{\sqrt{2}/2}} \bullet v_c^{\sqrt{2}/2} - 0.19 \bullet 10^4 \; \frac{\mathrm{W}}{\mathrm{mm}} \\ & \bullet d_t - 0.08 \frac{\mathrm{W}}{^\circ\mathrm{deg}} \bullet \zeta_\Phi \; + \; 0.24 \bullet 10^5 \; \frac{\mathrm{W} \bullet (\mathrm{m} \bullet \mathrm{K})^{-1/2}}{(\mathrm{W})^{-1/2}} \\ & \bullet (k_1 \bullet k_{33})^{-1/2} \; + \; 0.41 \bullet 10^{-3} \; \frac{\mathrm{W} \bullet \mathrm{kg} \bullet \mathrm{K} \bullet \mathrm{m}^3}{\mathrm{J} \bullet \mathrm{kg}} \bullet C_p \\ & \bullet \rho - 0.53 \bullet 10^{-1} \; \frac{\mathrm{W} \bullet \mathrm{min} \bullet \mathrm{mm}}{\mathrm{m} \bullet \mathrm{mm}} \bullet \frac{v_c \bullet f}{d_t} \; + \; 0.49 \\ & \bullet 10^3 \; \frac{\mathrm{W} \bullet \mathrm{m}^3}{\mathrm{MJ}} \; W_{el} \; + \; 0.51 \; \frac{\mathrm{W}}{\mathrm{W}} \bullet P_{th,eff} \end{aligned} \tag{14}$$

with the corresponding $R^2 = 0.89$. The confidence intervals at the 95 % confidence level of the appropriate coefficients are given in Table 6. For the dependencies listed, the limit for the p-value in the calculation of the coefficients was set to 0.05.

Table 6
Coefficients of the heat flow P_{HS} nonlinear regression model.

Predictor	Estimate	95 % CI (Lower, Upper)
β_0	$0.18 \bullet 10^4$	[1815.894, 1816.478]
β_1 (f)	$0.29 \bullet 10^3$	[292.163, 292.259]
β_2 ($v_c^{\sqrt{2}/2}$)	0.249	[0.132, 0.367]
β_3 (d_t)	$-0.19 \bullet 10^4$	$[-0.194, -0.193] \bullet 10^4$
β_4 (ζ_Φ)	– 0.08	[–0.105, –0.046]
β_5 ($(k_1 \bullet k_{33})^{-1/2}$)	$0.24 \bullet 10^5$	[24192.304, 24292.626]
β_6 ($C_p \bullet \rho$)	$0.41 \bullet 10^{-3}$	$[0.399, 0.426] \bullet 10^{-3}$
β_7 ($\frac{v_c \bullet f}{d_t}$)	$-0.53 \bullet 10^{-1}$	$[-0.702, -0.36] \bullet 10^{-1}$
β_8 (W_{el})	$0.49 \bullet 10^3$	$[0.486, 0.487] \bullet 10^3$
β_9 ($P_{th,eff}$)	0.51	[0.222, 0.791]

From the Eqs. (13) and (14) it can be seen, that most common predictors have similar influence on both the heat flow P_{HS} and the thermal contact length s_{HS}. Thus, the parameters considered increase with the feed f, product of the thermal capacity C_p and the density ρ, as well as the theoretical power of brittle fracture $P_{th,eff}$, and decrease with the fibre orientation symmetry angle ζ_Φ. The increase in tool diameter d_t, which was considered for the material CFRP 4, also leads to decrease of both the heat flow P_{HS} and the thermal contact length s_{HS}. It can be explained with a better heat removal by the bigger tool body as well as a higher cutting edge cooling time when not in engagement with the panel. Although a full factorial variation of the tool diameter d_t was not the case across the realized testing groups, this parameter was included in the resulting models based on the sufficient significance value of the corresponding coefficients.

Using the values of s_{HS} and P_{HS} calculated according to Eqs. (13, 14), the value of q_{HS} was calculated with the Eq. (5). A good correlation between the analytically determined thermal parameters s_{HS}, P_{HS} and q_{HS}, according to Eqs. (2–4) and those calculated empirically with Eqs. (13, 14) and using Eq. (5) is depicted in Fig. 7. The corresponding coefficients of determination for the linear regression shown in Fig. 7 are $R^2 = 0.9$ for s_{HS}, $R^2 = 0.87$ for P_{HS}, and $R^2 = 0.8$ for q_{HS}.

Compared to the phenomenological models presented in [28], the models developed in this study enable consideration not only of the processing parameters but also of the thermal and mechanical properties of the CFRP material. In addition to the possibilities provided by the previously known approaches [13,21,28,29,37], the developed phenomenological models allow it to determine not only the maximum temperature reached, but give the thermal process parameters q_{HS} and s_{HS} relevant to the overall cutting process depending on both material properties and cutting conditions, which in combination with the model in Eq. (2) reveals the temperature fields and therefore the thermally damaged zone of the CFRP panel, as well as provides these dependencies not only on the cutting parameters, but on the fibre orientation direction and thermal and mechanical properties of the material.

3.6. Simulation of temperature fields

According to the computational procedure described above, once the thermal parameters, the equivalent heat flux q_{HS} and the thermal contact length s_{HS}, are determined based on both the known cutting parameters and material properties with the help of the phenomenological models in Eqs. (13, 14) and the analytical Eq. (5), it becomes possible to calculate the temperature fields in the machined panels. These fields are tailored precisely to the specific cutting conditions. Several examples of such temperature fields are presented in Fig. 8.

The temperature fields in Fig. 8 are represented by color, with the matrix glass transition temperature T_g indicated in the color legends. Corresponding isolines are shown within the temperature fields, delineating the heat-affected zones (HAZ), where the temperature exceeds T_g, from the surrounding non affected regions. Not only the maximum temperature changes, but also the shapes of the temperature fields and thus the geometry of HAZ vary significantly depending on the fibre orientation angle Φ. The highest maximum temperature changes are observed for $\Phi = 135°$, consistent with the findings in [13,23]. But additionally, the optimal heat dissipation regions of unidirectional CFRP, as discussed in [13,49], can result in increased heat penetration depth along the fibres, thereby elongating the HAZ in that direction.

HAZ can be characterized in its length Δx_{HAZ}, i.e., extension along the cutting path, and its depth Δz_{HAZ} in direction normal to the machined surface. The former is important as it indicates duration $\Delta t_{HAZ} = \Delta x_{HAZ}/v_f$ of the temperature action at the same feed rate. E.g., in Fig. 8, the lengths of HAZ for CFRP 1 and 4 at $\Phi = 135°$ exceed the corresponding values for $\Phi = 45°$ and 90°. The influence of the time duration of exceeding the glass transition temperature T_g on the

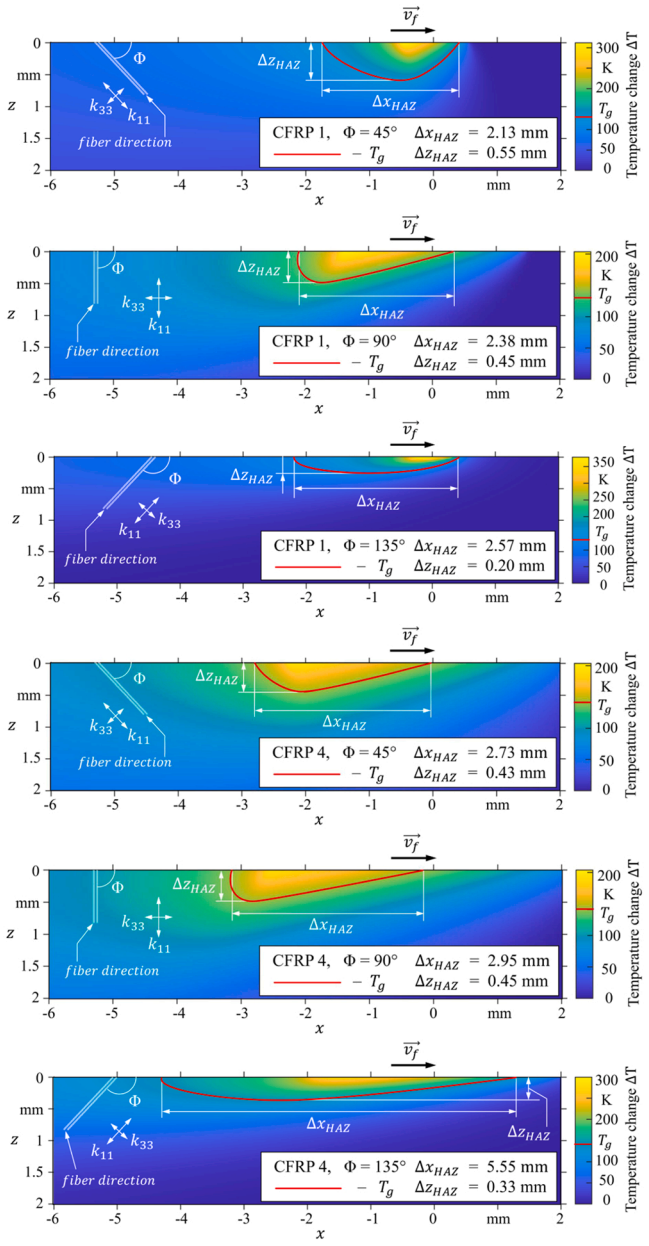

Fig. 8. Temperature fields in the machined panels for two tested materials, CFRP 1 and CFRP 4, in the same test series TS-II (please see Table 3 for the cutting parameters) for three different fibre orientation angles, $\Phi = 45°$, $\Phi = 90°$, and $\Phi = 135°$.

resulting strength and processed material properties as well as on delamination and damage during machining requires further detailed investigation. In this context, the shape of HAZ becomes particularly important, whereas not only the width of the HAZ at the machined surface, $\Delta x_{HAZ}(z = 0)$, but also the width at various depths, $\Delta x_{HAZ}(z > 0)$, are significantly different depending on the fibre orientation angle Φ. The gradient of the HAZ width decrease $d(\Delta x_{HAZ})/dz$, is lower for $\Phi = 45°$ and 90°, which can facilitate the development of deeper cracks and fracture craters at the machined surface, which are known from [9,10,12].

Another important aspect is the skewness of the HAZ, i.e., how the center of HAZ Δx_{HAZ} at each depth $z > 0$ is shifted relative to Δx_{HAZ} at $z = 0$. Depending on Φ, this shift determines whether cutting occurs in already preheated material, as in the case of $\Phi = 45°$, or in still unaffected, undeteriorated material. This observation supports the experimental findings of [43], where the boundary of the HAZ tended to align with the fibre direction due to anisotropic heat conduction.

In [16] the heat penetration depth corresponding to the glass transition temperature at $v_f = 0.4$ m/min is found to be in the range of 0.33 to 0.43 mm. This corresponds to the values of Δz_{HAZ} indicated in Fig. 8 for the current research.

When comparing these results with the findings reported in [6,8], it becomes clear that thermal considerations impose an additional constraint on the proper selection of optimal cutting parameters. Thus, the procedure described here is capable of modeling maximal surface temperatures and heat distribution in milling of UD CFRP.

4. Summary and outlook

The influence of material properties on the thermal performance of machining process was investigated in upcut milling for four UD-CFRPs of differing composition under three sets of cutting parameters and for three different fibre orientation angles. The thermal parameters were analyzed based on experiments and simulations using analytical and empirical models. The findings can be summarized as follows:

- semi-analytical model for heat flow and temperature field in CFRP milling developed;
- model valid for arbitrary unidirectional brittle CFRP materials and fibre orientations;
- thermal properties and specific elastic energy of CFRP materials considered;
- glass transition temperature at the machined surface mostly exceeded;
- dimension and shape of the heat affected zone predictable.

Irrespective of the material, the highest ΔT_{max} are observed at the fibre orientation angle $\Phi = 135°$.

Irrespective of the material, the glass transition temperatures of the matrices T_g were exceeded in all test series at the fibre orientation angle $\Phi = 135°$.

The differences in thermal as well as mechanical properties of investigated CFRP materials provide complicated mutual effects leading to non-uniform dependencies of temperature changes on the test series and fibre orientation angles.

Higher cutting speed v_c correlates to higher ΔT_{max} in most materials irrespective of full or partial cut.

All tested materials demonstrate a similar relation between the heat flow P_{HS}, cutting power P_c, and heat flow ratio R_W.

Apart from the thermal material properties, the mechanical properties, namely the specific elastic energy at fracture W_{el}, as well as the theoretical power of brittle fracture $P_{th,eff}$, which includes the influence of cutting conditions, are indispensable for modelling the thermal process parameters s_{HS}, q_{HS}, P_{HS}.

Considering the effective widths of cut $a_{e,eff}$ is necessary to properly evaluate the theoretical power of brittle fracture $P_{th,eff}$, whereas $a_{e,eff}$ is up to now determined experimentally.

Thermal parameters s_{HS}, q_{HS}, P_{HS} can be empirically modelled for arbitrary brittle unidirectional CFRP materials fibre orientation angles, and cutting conditions with a good correlation. The approach presented makes it possible to specifically determine cutting parameters for machining that are both highly productive and remain within thermally permissible limits. In the future, the influence of heat dissipation due to radiation from the side panel surface and from the machined surface as well as material parameters temperature dependencies and thermal parameters evaluation for multilayered composites should be considered. Special attention should be given to extending the model to multilayered laminates with varying fibre orientations, where interlayer thermal coupling must be considered. A similar approach can be applied to multidirectional CFRP structures by representing each multidirec-

tional layer as a set of thermally coupled unidirectional subsystems. Each of these subsystems can be characterized by its own thermal properties.

CRediT authorship contribution statement

Wolfgang Hintze: Conceptualization, Methodology, Validation, Investigation, Writing - Original Draft, Writing - Review & Editing, Supervision, Project administration, Funding acquisition. **Ganna Shchegel:** Software, Validation, Formal analysis, Investigation, Data Curation, Writing - Original Draft, Visualization. **Jan Mehnen:** Conceptualization, Methodology, Software, Funding acquisition. **Carsten Möller:** Resources, Data Curation, Writing - Original Draft, Supervision, Project administration, Funding acquisition. **Jan Dege:** Validation, Writing - Review & Editing, Supervision, Project administration.

Declaration of Competing Interest

The authors declare that they have no known competing financial interests or personal relationships that could have appeared to influence the work reported in this paper.

Acknowledgements

We would like to acknowledge and cordially thank the German Research Foundation DFG for funding support of the project 461768523 GZ: HI 843/14–1 AOBJ: 679098.

References

[1] Hintze W. CFK-Bearbeitung: Trenntechnologien für Faserverbundkunststoffe und den hybriden Leichtbau. Berlin Heidelberg: Springer; 2021. https://doi.org/10.1007/978-3-662-63265-9.
[2] Geier N, Xu J, Poór DI, Dege JH, Davim JP. A review on advanced cutting tools and technologies for edge trimming of carbon fibre reinforced polymer (CFRP) composites. Compos B Eng 2023;266:111037. https://doi.org/10.1016/j.compositesb.2023.111037.
[3] Slamani M, Châtelain JF. A review on the machining of polymer composites reinforced with carbon (CFRP), glass (GFRP), and natural fibers (NFRP). Discov Mech Eng 2023;2. https://doi.org/10.1007/s44245-023-00011-w.
[4] Che D, Saxena I, Han P, Guo P, Ehmann KF. Machining of carbon fiber reinforced plastics/polymers: a literature review. J Manuf Sci Eng 2014;136:034001. https://doi.org/10.1115/1.4026526.
[5] Hou G, Luo B, Zhang K, Luo Y, Cheng H, Cao S, et al. Investigation of high temperature effect on CFRP cutting mechanism based on a temperature controlled orthogonal cutting experiment. Compos Struct 2021;268:113967. https://doi.org/10.1016/j.compstruct.2021.113967.
[6] Espilla I, Telleria M, Llanos I, Norberto L. Experimental study on drilling machinability of CFRP: tool geometry, hole quality and process monitoring analysis. Proc CIRP 2025;131:80–5. https://doi.org/10.1016/j.procir.2024.09.016.
[7] Rech J, Arrazola P, Claudin C, Courbon C, Pusavec F, Kopac J. Characterisation of friction and heat partition coefficients at the tool-work material interface in cutting. CIRP Ann 2013;62:79–82. https://doi.org/10.1016/j.cirp.2013.03.099.
[8] Beuscart T, Arrazola P-J, Tinel N, Ducobu F. Effect of cutting conditions on surface integrity when robotic drilling of aluminum 6082-GFRP stacks. Procedia CIRP 2024;123:428–33. https://doi.org/10.1016/j.procir.2024.05.075.
[9] Zhang L, Zhang X. A comparative experimental study of unidirectional CFRP high-speed milling in up and down milling with varied angles. J Manuf Process 2023;101:1147–57. https://doi.org/10.1016/j.jmapro.2023.06.064.
[10] Brouschkin A, Köttner L, Hintze W, Dege J. Prediction of surface profile in CFRP machining through phenomenological analysis and inverse continuous wavelet transformation. Proc CIRP 2024;123:143–8. https://doi.org/10.1016/j.procir.2024.05.027.
[11] Ozkan D, Panjan P, Gok M, Karaoglanli A. Experimental study on tool wear and delamination in milling CFRPs with TiAlN- and TiN-coated tools. Coatings 2020;10:623. https://doi.org/10.3390/coatings10070623.
[12] Cai C, Dang J, Ming AaQ, Chen W. M. Surface morphology characterization of unidirectional carbon fibre reinforced plastic machined by peripheral milling. Chin J Aeronaut 2022;35:361–75. https://doi.org/10.1016/j.cja.2021.04.024.
[13] Wang H, Sun J, Zhang D, Guo K, Li J. The effect of cutting temperature in milling of carbon fiber reinforced polymer composites. Compos A Appl Sci Manuf 2016;91:380–7. https://doi.org/10.1016/j.compositesa.2016.10.025.
[14] Castillo-Morales A, Rimpault X, Chatelain J-F, Lebrun G. Temperature study during the edge trimming of carbon fiber-reinforced plastic [0]8/Ti6Al4V stack material. J Compos Sci 2021;5:137. https://doi.org/10.3390/jcs5050137.
[15] Yashiro T, Ogawa T, Sasahara H. Temperature measurement of cutting tool and machined surface layer in milling of CFRP. Int J Mach Tools Manuf 2013;70:63–9. https://doi.org/10.1016/j.ijmachtools.2013.03.009.
[16] Sheikh-Ahmad J, Almaskari F, Hafeez F. Thermal aspects in machining CFRPs: effect of cutter type and cutting parameters. Int J Adv Manuf Technol 2019;100:2569–82. https://doi.org/10.1007/s00170-018-2881-1.
[17] Khashaba U, Abd-Elwahed M, Najjar I, Melaibari A, Ahmed K, Zitoune R, et al. Heat-affected zone and mechanical analysis of GFRP composites with different thicknesses in drilling processes. 2246–2246 Polymers 2021;13. https://doi.org/10.3390/polym13142246.
[18] Kerrigan K, O'Donnell G. On the relationship between cutting temperature and workpiece polymer degradation during CFRP edge trimming. Proc CIRP 2016;55:170–5. https://doi.org/10.1016/j.procir.2016.08.041.
[19] Ghafarizadeh S, Lebrun G, Chatelain J. Experimental investigation of the cutting temperature and surface quality during milling of unidirectional carbon fiber reinforced plastic. J Compos Mater 2015;50:1059–71. https://doi.org/10.1177/0021998315587131.
[20] Luchesi V, Coelho R. An inverse method to estimate the moving heat source in machining process. Appl Therm Eng 2012;45-46:64–78. https://doi.org/10.1016/j.applthermaleng.2012.04.014.
[21] Mehnen J, Hintze W, Köttner L, von Wenserski R. Temperature field due to a moving heat source in machining orthotropic composites with arbitrary fiber orientation. Procedia CIRP 2019;85:2–7. https://doi.org/10.1016/j.procir.2019.09.019.
[22] Rodríguez A, Calleja A, de Lacalle LNL, Pereira O, Rubio-Mateos A, Rodríguez G. Drilling of CFRP-Ti6Al4V stacks using CO_2-cryogenic cooling. J Manuf Proc 2021;64:58–66. https://doi.org/10.1016/j.jmapro.2021.01.018.
[23] El-Hofy M, Soo S, Aspinwall D, Sim W, Pearson D, M'Saoubi R, et al. Tool temperature in slotting of CFRP composites. Proc Manuf 2017;10:371–81. https://doi.org/10.1016/j.promfg.2017.07.007.
[24] Zou F, Zhong B, Zhang H, An Q, Chen M. Machinability and surface quality during milling CFRP laminates under dry and supercritical CO_2-based cryogenic conditions. Int J Precis Eng Manuf Green Technol 2021;9:765–81. https://doi.org/10.1007/s40684-021-00386-9.
[25] Ge J, Fu G, Almeida Jr J, Jin Y, Sun D. Thermal effect in CFRP machining: temperature field characteristics, heat generation mechanism and thermal damage management. Comp Struct 2025;356:118845. https://doi.org/10.1016/j.compstruct.2025.118845.
[26] Liu L, Qu D, Wang J, Zhang J, Cao H, Dong X. Thermal-field analytical modeling of machined surface layer in high-speed-dry milling UD-CF/PEEK considering thermal anisotropy and nonlinear thermal conductivity. Compos A Appl Sci Manuf 2024;176:107864. https://doi.org/10.1016/j.compositesa.2023.107864.
[27] Jaeger JC. Moving sources of heat and the temperature at sliding contacts. J Proc R Soc NSW 1942;76:203–24.
[28] Elgnemi T, Songmene V, Kouam J, Jun M, Samuel A. Experimental investigation on dry routing of CFRP composite: temperature, forces, tool wear, and fine dust emission. 5697–5697 Materials 2021;14. https://doi.org/10.3390/ma14195697.
[29] Ni J, Liu H, Hong Z, Meng A, Li M. Research on multiscale modeling and experiment of CFRP milling. 6748–6748 Materials 2023;16. https://doi.org/10.3390/ma16206748.
[30] Qiu J, Zhang S, Li B, Li Y, Wang L. Research on tool wear and surface integrity of CFRPs with mild milling parameters. Coatings 2023;13.
[31] Du Y, Yang T, Liu C, Sun Y. Damage performance in drilling of carbon fiber-reinforced polyetheretherketone composites using drills with different geometries. Int J Adv Manuf Technol 2022;121:1743–53. https://doi.org/10.1007/s00170-022-09430-7.
[32] Mullier G, Chatelain JF. Influence of thermal damage on the mechanical strength of trimmed CFRP. Int J Mech Mechatron Eng 2015;9(8):1559–66. https://doi.org/10.5281/zenodo.1109525.
[33] Prakash R, Krishnaraj V, Tarun GS, Vijayagopal M, Kumar GD. Experimental study on temperature effect and tool wear on edge trimming of carbon fiber reinforced plastics. J Appl Mech Mater 2014;592–594:333–8. https://doi.org/10.4028/www.scientific.net/AMM.592-594.333.
[34] Ge J, Luo M, Zhang D, Catalanotti G, Falzon B, McClelland J, et al. Temperature field evolution and thermal-mechanical interaction induced damage in drilling of thermoplastic CF/PEKK – a comparative study with thermoset CF/epoxy. J Manuf Process 2023;88:167–83. https://doi.org/10.1016/j.jmapro.2023.01.042.
[35] Zenia S, Ben Ayed L, Nouari M, Delamézière A. Numerical analysis of the interaction between the cutting forces, induced cutting damage, and machining parameters of CFRP composites. Int J Adv Manuf Tech 2014;78:465–80. https://doi.org/10.1007/s00170-014-6600-2.
[36] An Q, Zhang J, Xiao G, Xu C, Yi M, Chen Z, et al. Fiber orientation effects in CFRP milling: multiscale characterization of cutting dynamics, surface integrity, and damage mechanisms. J Compos Sci 2025;9:342. https://doi.org/10.3390/jcs9070342.
[37] Hintze W, Shchegel G, Mehnen J, Möller C, Dege J. Modeling of temperature fields in milling of unidirectionally reinforced CFRP depending on the fibre orientation angle and the effective width of cut. Proc CIRP 2025;131:19–25. https://doi.org/10.1016/j.procir.2024.09.006.
[38] Hintze W, Shchegel G, Mehnen J, Möller C, Dege J. Model based assessment of maximal surface temperatures and heat flow in edge trimming of UD CFRP with tools of different type. Comp B Eng 2025;300:112483. https://doi.org/10.1016/j.compositesb.2025.112483.
[39] Gao T, Zhang Y, Li C, Wang Y, Chen Y, An Q, et al. Fiber-reinforced composites in milling and grinding: machining bottlenecks and advanced strategies. Front Mech Eng 2022;17. https://doi.org/10.1007/s11465-022-0680-8.

[40] Qian M, Xiao J, Wang G, Huang P, Chen Z, Han G. Evaluation of heat generation using a microscopic cutting model with thermo-mechanical coupling for carbon fiber reinforced polymer composites. J Reinf Plast Compos 2020;39:793–804. https://doi.org/10.1177/0731684420931589.
[41] Mkaddem A, Zain-ul-Abdein M, Mezlini S, Mahfouz A, Jarraya A. Sensitivity of GFRP composite integrity to machining-induced heat: a numerical approach. Appl Cond Monit 2016;5:205–14. https://doi.org/10.1007/978-3-319-41459-1_20.
[42] Saraireh M. A new approach for heat flux estimation in composite materials. 104371–1 Results Eng 2025;25. https://doi.org/10.1016/j.rineng.2025.104371.
[43] Wang F-j, Yin J-w, Ma J-w, Niu B. Heat partition in dry orthogonal cutting of unidirectional CFRP composite laminates. Compos Struct 2018;197:28–38.
[44] Resources | HexPly Prepreg Data Sheets. Hexcel. Hexcelcom 2025. https://www.hexcel.com/Resources/ (accessed April 9, 2025).
[45] Adibekyan A, Kononogova E, Monte C, Hollandt J. Review of PTB measurements on emissivity, reflectivity and transmissivity of semitransparent fiber-reinforced plastic composites. Int J Thermophys 2019;40. https://doi.org/10.1007/s10765-019-2498-0.
[46] Bentz D.P. Fire resistive materials: thermal barriers between fires and structures. Thermal Conductivity 30/Thermal Expansion 18, NIST; 2010, p. 1–12. https://tsapps.nist.gov/ publication/get_pdf.cfm?pub_id =902567.
[47] Sandten U., Hoffmann K., Teubner D., Weigel U., Reinhart W., Genzel L. Physik B. G. Teubner Verlag; 2007. https://doi.org/10.1007/978–3-8351–9201-0.
[48] Seber GA, Wild CJ. Nonlinear regression. Hoboken, NJ: Wiley-Interscience,; 2003.
[49] Hintze W, Schütte C, Steinbach S. Influence of the fiber cutting angle on work piece temperature in drilling of unidirectional CFRP. Lect Notes Prod Eng 2013:137–43. https://doi.org/10.1007/978-3-319-01964-2_19.